Supporting Information

High-performance anion exchange membrane fuel cells and zinc-air batteries enabled by a hierarchically porous hollow Fe/N/C aerogel catalyst

Liqiang Wang[1,2], Jiang Zhong[2], Yanqing Fu[2], Fen Wu[1*], Sen Wang[2], Jie Li[2], Han Yu[2], Qing Shi[2], Qiao Liu[2], Ruizhi Yu[2], Bing Wu[3], Zdenek Sofer[3], Kun Zheng[4], Weiyou Yang[2], and Qiliang Wei[1,2*]

[1]*College of Chemistry and Materials Engineering, Wenzhou University, Wenzhou 325000, P. R. China;*

[2]*Institute of Micro/Nano Materials and Devices, Ningbo University of Technology, Ningbo, 315211, P.R. China.*

[3] *Department of Inorganic Chemistry, University of Chemistry and Technology Prague, Technická 5, 166 28 Prague 6, Czech Republic*

[4] *Faculty of Energy and Fuels, AGH University of Krakow, Al. A. Mickiewicza 30, Krakow 30-059, Poland*

[*]Corresponding author emails: wufen@wzu.edu.cn (F.W.); qiliang.wei@nbut.edu.cn (Q.W.)

1. Materials synthesis

1.1 Chemicals

Iron(III) Nitrate Nonahydrate and 2-Methylimidazole (98%, Damas-beta), Hexahydrate Zinc Nitrate (>99%, Sinopharm Chemical Reagent Co., Ltd.), Nafion (5 wt%, mixture of lower aliphatic alcohols and water, Sigma-Aldrich), Pt/C (20 wt% Pt, TANAKA TEC10E20E), Methanol (Aladdin AR, 99.5%), Ethanol (Aladdin AR, 99.9%), KOH (Macklin, 90%), Carboxymethyl Cellulose I (Macklin), Acetone (analytical reagent grade, Sinopharm Chemical Reagent Co., Ltd.), PtRu/C (50% PtRu, 50% C, SINO-PLATINUM METALS CO., LTD, GJS-HK-KLP), Conductive Carbon Black (Super P Li, TIMCAL). The distilled water used in the experiment was of Milli-Q grade, with a specific resistance of 18.2 MΩ cm.

1.2 Fe/N/C catalyst synthesis

Zinc nitrate hexahydrate ($Zn(NO_3)_2 \cdot 6H_2O$, 2.0 g) and iron nitrate nonahydrate ($Fe(NO_3)_3 \cdot 9H_2O$, 120 mg) were completely dissolved in methanol solution (300 mL), and dimethyl imidazole (2-MI, 2.3 g) was dissolved in another methanol solution (300 mL). The two solutions were mixed and reacted in an oil bath at 60 ℃ for 1 h. The precipitate is separated and washed twice with methanol. Light yellow Fe^{3+}-ZIF-8 powder was obtained after overnight vacuum drying at 70 ℃.

Fe^{3+}-ZIF-8 powder was heated in an N_2 atmosphere for 2 h at 1100 ℃, and finally, the black powder was named Fe/N/C.

1.3 FeN-CA catalyst synthesis

Fe^{3+}-ZIF-8 powder was dissolved in acetone aqueous solution (V:V = 1:20, 5 mL) and ultrasonic for 3 h. Carboxymethyl cellulose (CMC) was dissolved in aqueous solution (5 mL) at 80 ℃ and stirred at room temperature for 3 h. The two solutions were mixed and stirred for 3 h, and the light-yellow hydrogel was obtained by ultrasound for 3 h. Pre-frozen at -19 ℃ overnight, and then freeze-dried for 48 h to obtain light yellow aerogel. Aerogels of different proportions were obtained by changing the mass ratio of Fe^{3+}-ZIF-8 powder. The aerogels were heated at 1100 ℃ in an N_2 atmosphere for 2 h, and black powder FeN-CA was obtained. The mass ratio of

Fe^{3+}-ZIF-8 to CMC is adjusted and denoted as X:Y FeN-CA, where X:Y represents the ratio of Fe^{3+}-ZIF-8 to CMC, to prepare a series of catalysts.

2. Characterization

The morphology and microstructure of the sample were characterized using a Field Emission Scanning Electron Microscope (SEM) (S-4800, Hitachi Global) and a High-Resolution Transmission Electron Microscope (TEM) (JEM-2100F, JEOL) equipped with Energy-Dispersive X-ray Spectroscopy (EDX, Bruker) (Quantax STEM). Powder X-ray diffraction patterns were collected within a 2θ range of 10°-70° on a Bruker D8 Focus X-ray diffractometer equipped with a Cu Kα radiation source (λ=1.5406 Å). Additionally, Raman spectroscopy (Raman, Renishaw in Via, UK) with a 532 nm excitation laser was employed to evaluate the phase composition. Nitrogen (N_2) adsorption-desorption isotherms were collected at 77 K on a BSD-660M A3M|B3 machine. The specific surface area (SSA) was calculated using the BET model based on adsorption data within the pressure range of P/P_0 = 0 to 1. The pore size distribution was analyzed using the DFT model from the adsorption branch of the isotherm. Chemical states were measured by X-ray Photoelectron Spectroscopy (XPS) (ES-CALAB 250 Xi, Thermo Fisher Scientific), calibrated using the carbon peak (C1s) at 284.8 eV. X-ray Absorption Spectroscopy (XAS), including X-ray Absorption Near Edge Structure (XANES) and Extended X-ray Absorption Fine Structure (EXAFS), at the Fe K-edge of the sample was collected at the TLS07A1 beamline of the National Synchrotron Radiation Research Center in Taiwan, operating in the fluorescence mode.

3. Electrochemical measurement

All the electrochemical tests were performed on a CHI 760E electrochemical station (Shanghai Chen Hua Instrument Co. Ltd.) in a three-electrode cell used to perform all measurements on all catalysts in 0.1 M KOH solution at room temperature. Using an Hg/HgO electrode (saturated with 1 M KCl) and a graphite rod respectively as the reference electrode and the counter electrode, with a glassy carbon rotating ring-disk electrode (RRDE) coated with catalyst ink serving as the working electrode. All

potentials in this work are referenced to the reversible hydrogen electrode (RHE), which was measured using an Hg/HgO reference electrode and a Pt sheet working electrode in an electrolyte saturated with hydrogen. The catalyst ink was prepared by ultrasonically dispersing 10 mg catalyst into a solution containing 95 μL Nafion and 350 μL ethanol. The 9 μL ink was applied to the surface of the polished glassy carbon electrode, and the catalyst support of ~ 0.8 mg cm^{-2} was obtained by natural air drying. Before the test, pure O_2 (99.999%) or N_2 (99.999%) gas was injected into the electrolyte for about 30 min to obtain saturated O_2 or N_2 solution. Cyclic voltammetry curves (CV, 50 mV s^{-1}) were tested in a N_2 saturated 0.1 M KOH solution, and linear voltammetry curves (LSV, 10 mV s^{-1}) were tested in an O_2 saturated 0.1 M KOH solution and in the 0 to 1.2 V vs. RHE range at 1600 rpm and 5 mV s^{-1}. N_2 saturation in the same electrolyte test background, the difference between the two is the true oxygen reduction current. The electron transfer number and hydrogen peroxide yield of the catalyst are measured by RRDE, and the equation is as follows:

$$n = \frac{4I_D}{I_D + (I_R/N)}$$

$$H_2O_2\,\% = 100\frac{2I_R/N}{I_D + (I_R/N)}$$

Where I_D is the disk current, I_R is the ring current, N is the collection coefficient, and N = 0.38 is determined by the REDOX of potassium ferricyanide/potassium ferricyanide. The kinetic current density (J_K) is obtained by the Koutecky-Levich equation:

$$\frac{1}{J} = \frac{1}{J_L} + \frac{1}{J_K} = \frac{1}{Bw^{1/2}} + \frac{1}{J_K}$$

Levich equation:

$$J_L = Bw^{1/2} = 0.62nFD^{\frac{3}{2}}v^{-\frac{1}{6}}C_0\omega^{\frac{1}{2}}$$

In the Koutecky-Levich equation, J is the current density measured from the ORR,

J_K is the kinetic current density, J_L is the limiting current density. In the Levich equation, n is the number of electrons involved in the oxidation reaction, F is the Faraday constant, D is the diffusion coefficient of the reactant, v is the viscosity of the electrolyte, C_0 is the solubility of O_2 in the electrolyte, B is the Levich constant, and ω is the rotation speed.

Catalyst stability was evaluated by performing the LSV before and after different numbers of CV scans (0.6-1.2 V in O_2-saturated KOH electrolyte).

The H_2O_2 resistance experiment was conducted using chronoamperometry at a potential of -0.3 V vs. Hg/HgO in a 0.1M KOH solution saturated with O_2.

The double-layer capacitance (C_{dl}) is obtained from the double-layer charging curve tested in the non-Faradaic potential range of 0.55-0.65 V vs. RHE. The electrochemically active surface area (ECSA) is calculated based on the following formula:

$$ECSA = \frac{C_{dl}}{C_{GDE} \times m_{cata}}$$

C_{GDE} refers to the double-layer capacitance of GCE (0.02 mF cm^{-2}) and m_{cata} represents the catalyst loading (8 g m^{-2})[1].

4. AEMFC assembly and tests.

Membrane electrode assembly (MEA) was prepared via catalyst-coated membrane (CCM) method. Specifically, catalysts and ionomer (PiperION-A5-HCO3 at 5 wt%) were added to a methanol/water mixture in a ratio of 3/1, with an anode ionomer-to-catalyst (I/C) ratio of 85%/15% and a cathode I/C ratio of 70%/30%. The mixture was stirred for 1 hour and then sonicated at room temperature for 2 hours to obtain uniformly mixed anode and cathode catalyst inks. A PtRu (50%)/C catalyst with a loading of 0.6 mg cm^{-2} was sprayed as the anode catalyst onto one side of a 20 μm thick PiperION-A20-HCO3 anion exchange membrane (AEM). The cathode catalyst was a mixture of 14:1 FeN-CA catalyst and conductive carbon black in a 1:1 mass ratio, with a loading of 1 mg cm^{-2} for FeN-CA. These catalyst inks were sprayed onto the other side of the AEM using an ultrasonic sprayer (Cheersonic), with an effective membrane area of 5

cm^2. The CCM was then soaked in a 1M KOH aqueous solution for 2 hours, with the solution replaced every hour. Suitable gaskets and gas diffusion layers (GDL, Sigracet 22 BB) were selected and sandwiched around the CCM. The assembly was compressed into a cell with a torque of 5 Nm, achieving a compression rate of 20% to 25%.

The AEMFC test setup was assembled using a fuel cell test station (Scribner 850g) and a backpressure regulation device. The cell temperature was set to 80 ℃, and the humidity at the anode and cathode was adjusted by varying their respective gas temperatures, while the backpressure was controlled using the backpressure regulation device. The anode and cathode gases were O_2/H_2 (99.999 %) with a flow rate of 0.5 mL min^{-1} for each. Polarization curves were tested by controlling the potential from open-circuit voltage (OCV) to 0.2 V at a scan rate of 10 mV s^{-1}.

4. ZAB assembly and tests.

To prepare a uniform catalyst ink, either 14:1 FeN-CA or Fe/N/C catalyst (2.5 mg), along with Nafion (50 μL), was dispersed in 0.5 mL of ethanol and subjected to ultrasonic treatment for 20 minutes. A precise volume of this ink was then drop-cast onto a 1.5 cm × 1.5 cm carbon paper to achieve a mass loading of 0.5 mg cm^{-2}. After natural air-drying, a catalyst-loaded gas diffusion layer (GDL) was formed. The GDL was compressed onto nickel foam to serve as the air cathode, while a polished zinc plate with a thickness of 0.2 mm was utilized as the anode. A zinc-air battery was assembled using a 6M KOH aqueous solution as the electrolyte. Polarization curves were obtained on a Cortest electrochemical workstation (CT2350H) at temperatures of 25 °C and 80 °C, within a voltage range of 1.5 V to 0.5 V, at a scan rate of 5 mV s^{-1}. Rate capability tests were conducted using the LAND CT2001A battery testing system at various current densities (2 mA cm^{-2}, 4 mA cm^{-2}, 6 mA cm^{-2}, 8 mA cm^{-2}, 10 mA cm^{-2}, and 20 mA cm^{-2}).

6. Finite-element method simulations

Model Construction: Based on scanning electron microscope (SEM) and transmission electron microscope (TEM) images, the concave dodecahedron is simplified into a regular hexagonal star. For the open-pore hollow carbon particles: (a)

the outer edge length of the model is 100 nm, with a thickness of 20 nm. The inward-facing hexagonal star features six openings, each with a width of 40 nm and a depth of 30 nm. Assuming a tight arrangement of the porous carbon particles (4 × 6 in total), the overall model is depicted as shown in the Figure S12. The gray areas in the figure represent the solid portions of the open-pore carbon particles, while the remaining parts represent pores. For the solid carbon particles, (b) their overall dimensions match those of the open-pore hollow carbon particles (Figure S16).

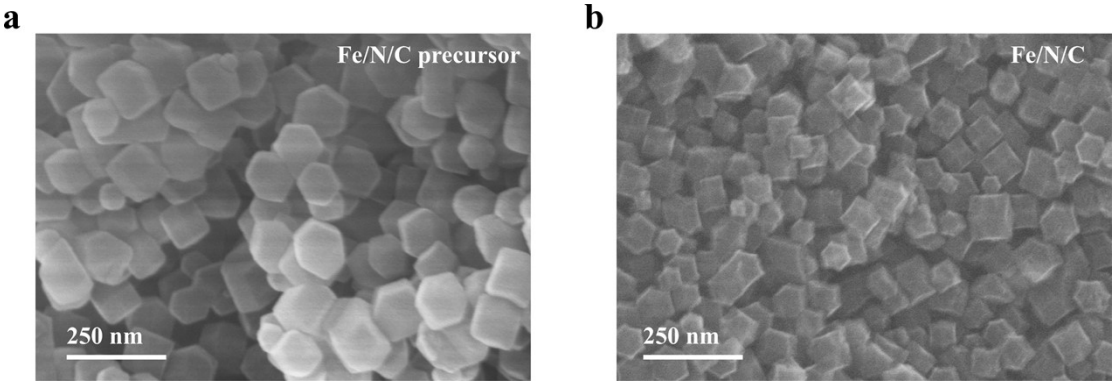

Figure S1. SEM images of a) Fe/N/C precursors and b) Fe/N/C carbonized at 1100 ℃.

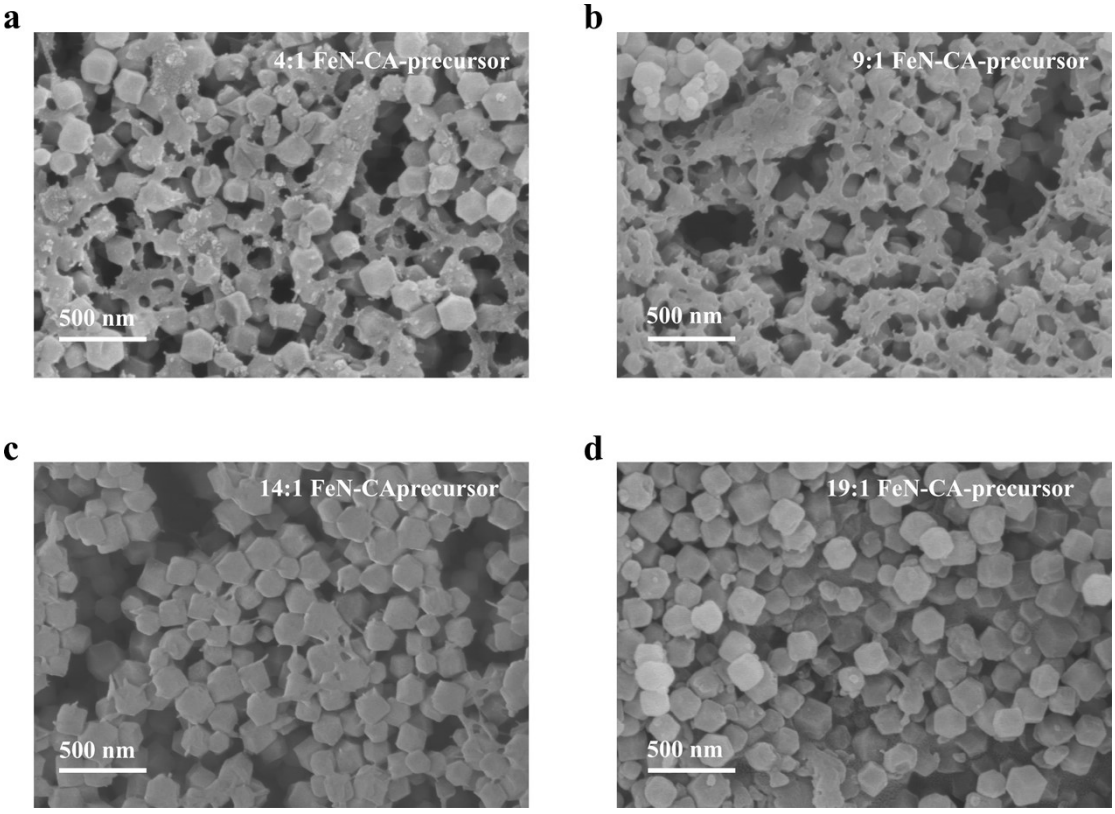

Figure S2. SEM images of FeN-CA precursors with different proportions (Fe^{3+}/ZIF-8: CMC).

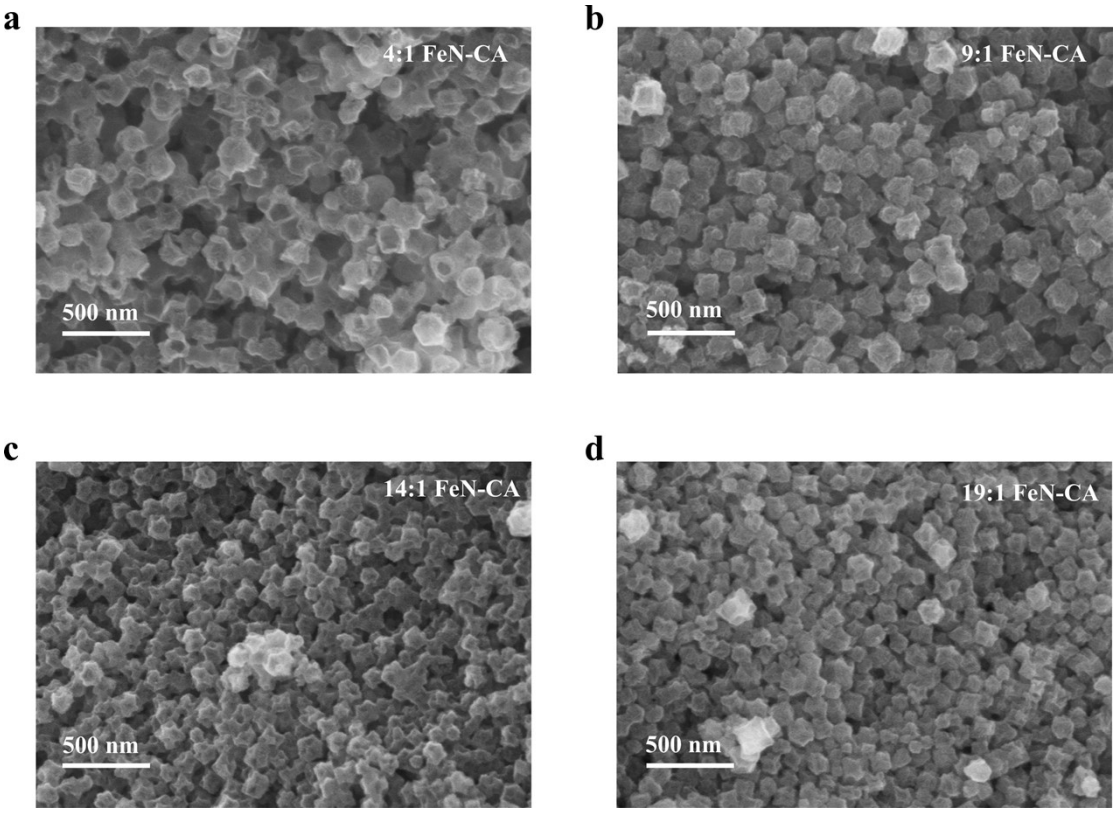

Figure S3. SEM images of different proportions of FeN-CA catalysts carbonized at 1100 ℃.

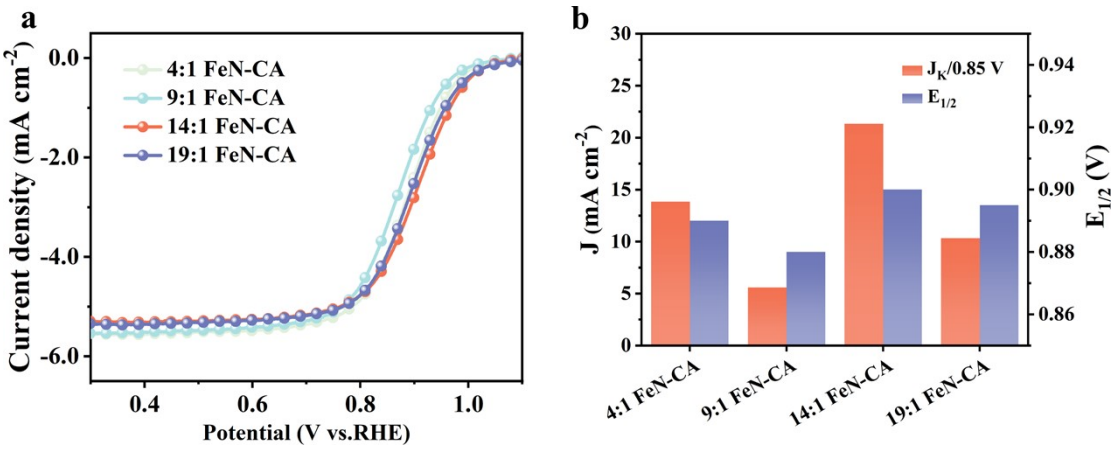

Figure S4. ORR performance of FeN-CA catalyst (800 μg cm^{-2}) with different proportions at 0.1 M KOH, 25 ℃ and 1600 rpm. a) LSV curve; b) J_K at 0.85 V and $E_{1/2}$.

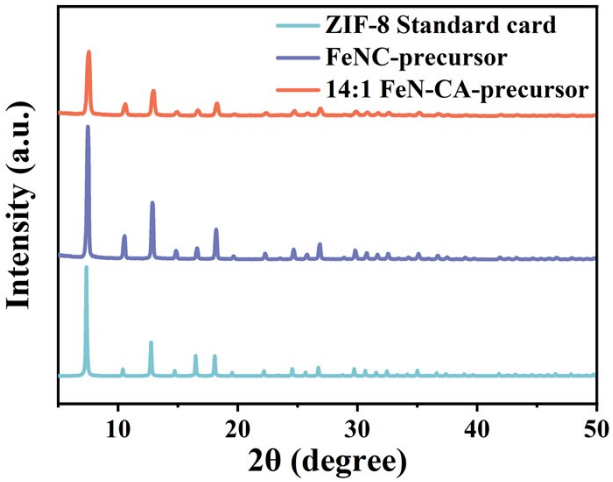

Figure S5. X-ray diffraction (XRD) patterns of the Fe/N/C precursor and 14:1 FeN-CA precursor.

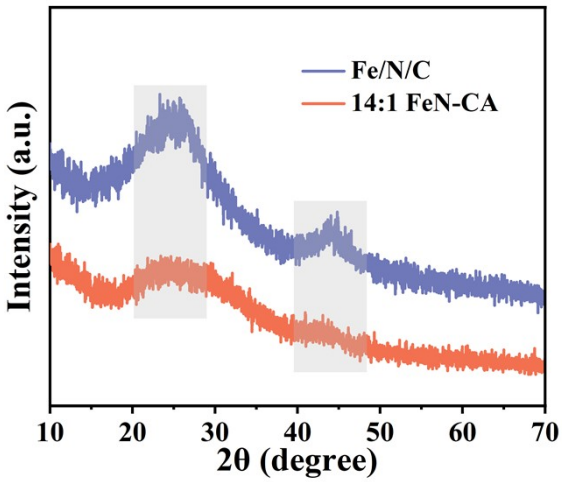

Figure S6. X-ray diffraction (XRD) patterns of the Fe/N/C catalyst and 14:1 FeN-CA catalyst.

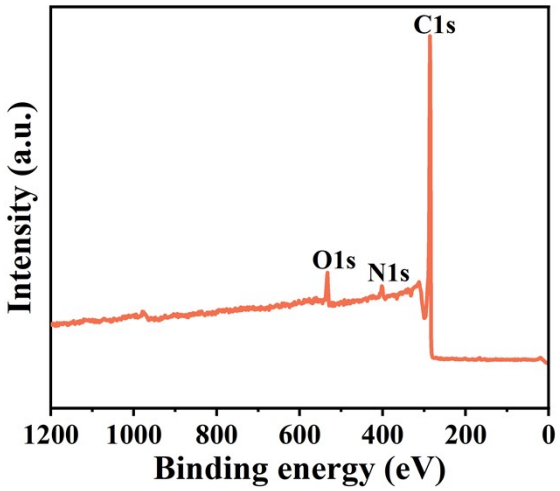

Figure S7. XPS full spectrum of 14:1 FeN-CA catalyst.

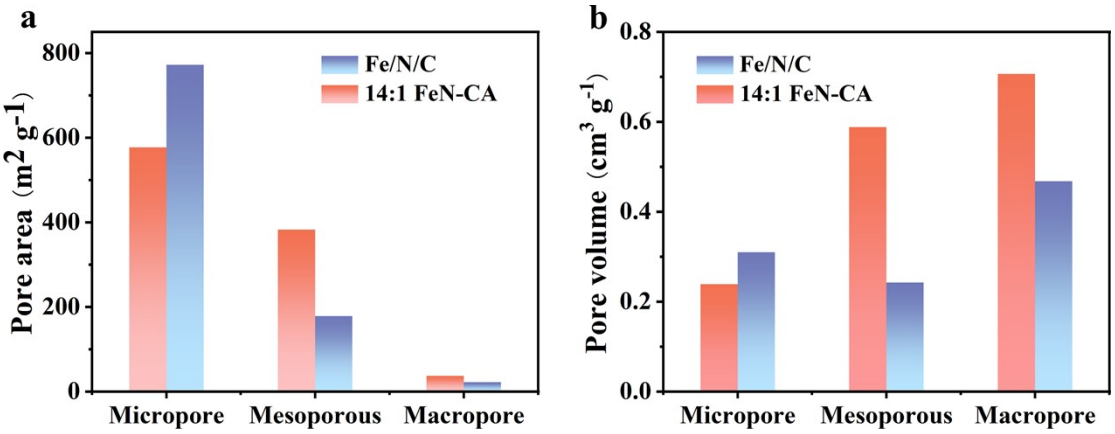

Figure S8. Specific surface area a) and pore volume b) of Fe/N/C and 14:1 FeN-CA catalyst at different pore structures.

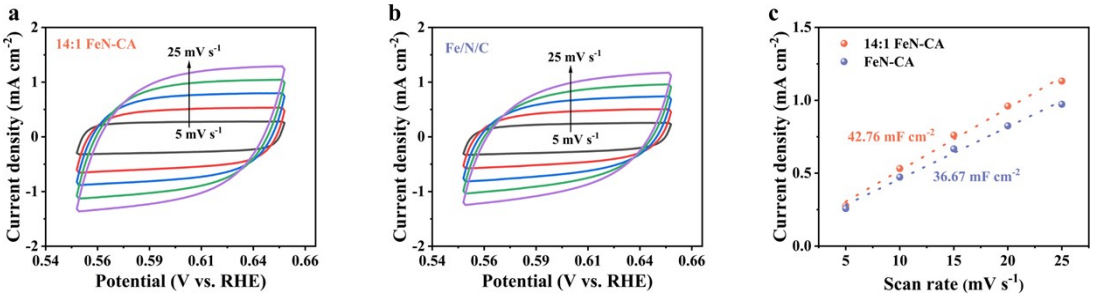

Figure S9. (a-b) Cyclic voltammetry (CV) curves within the potential range of 0.55-0.65 V vs. RHE at various scan rates, along with the corresponding linear fitting of capacitive currents versus scan rates, which is used to estimate the double-layer capacitance (C_{dl}). (c) The relationship between scan rate and current density for the catalyst at a potential of 0.6 V vs. RHE.

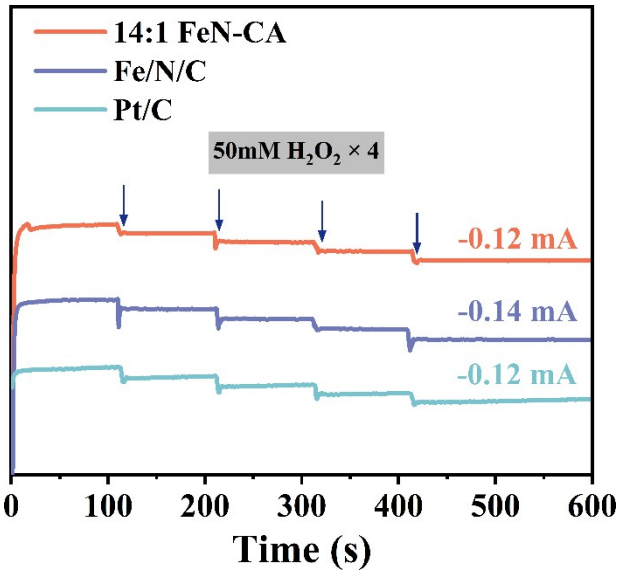

Figure S10. Experiment on H_2O_2 tolerance of 14:1 FeN-CA, Fe/N/C, and Pt/C catalysts.

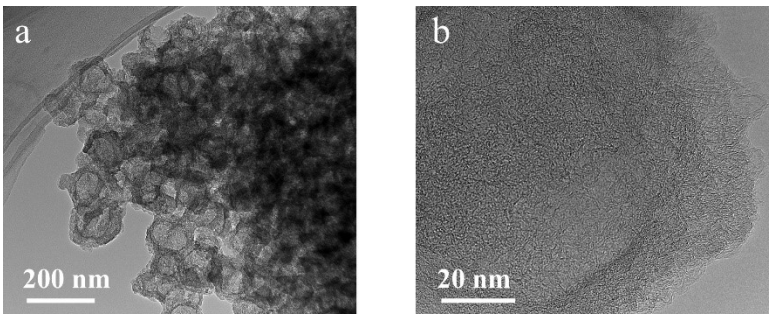

Figure S11. a) TEM image of the 14:1 FeN-CA sample after 10,000 CV cycles. b) High-resolution TEM image of the same sample after 10,000 CV cycles.

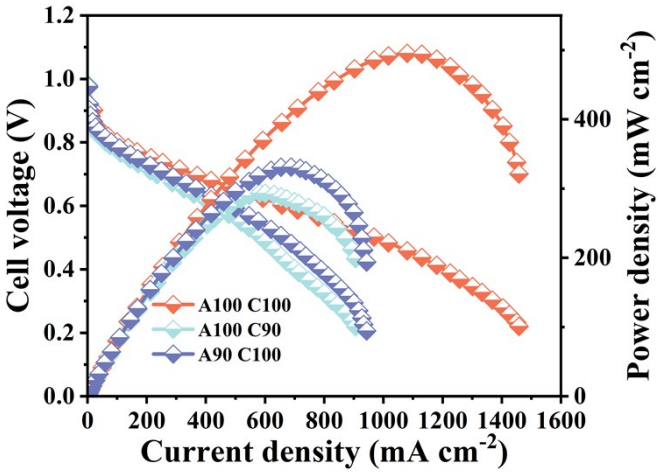

Figure S12. AEMFC performance of 14:1 FeN-CA at different humidity (The back pressure of cathode and anode is 0 bar).

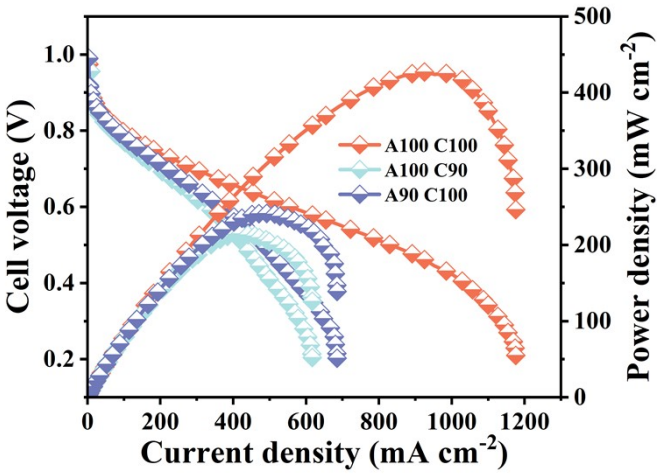

Figure S13. AEMFC performance of Fe/N/C at different humidity (The back pressure of cathode and anode is 0 bar).

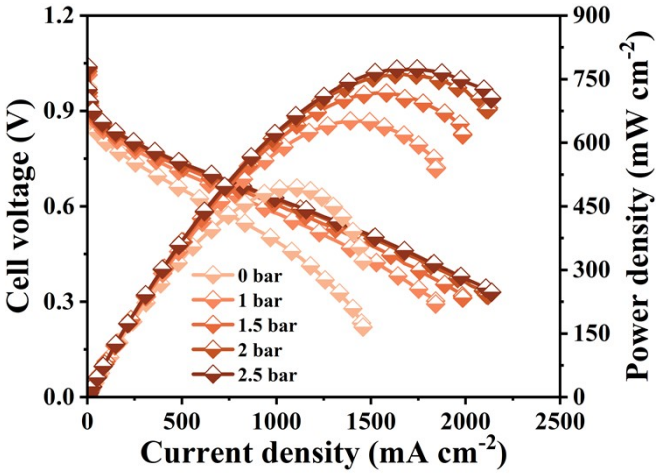

Figure S14. AEMFC performance at 14:1 FeN-CA at different back pressures (cathode and anode humidity of 100% RH).

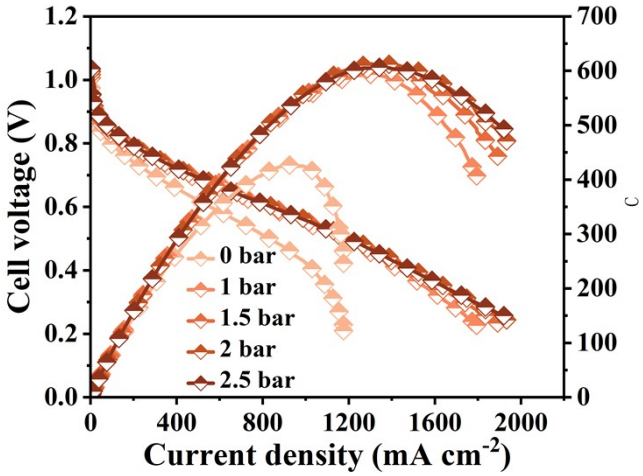

Figure S15. AEMFC performance of Fe/N/C at different back pressures (cathode and anode humidity of 100% RH).

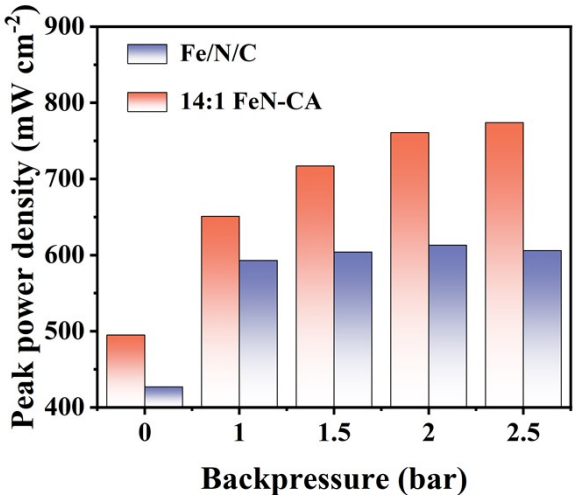

Figure S16. Comparison of peak power density (PPD) of Fe/N/C and 14:1 FeN-CA catalysts at different back pressures (100% RH for both cathode and anode humidity).

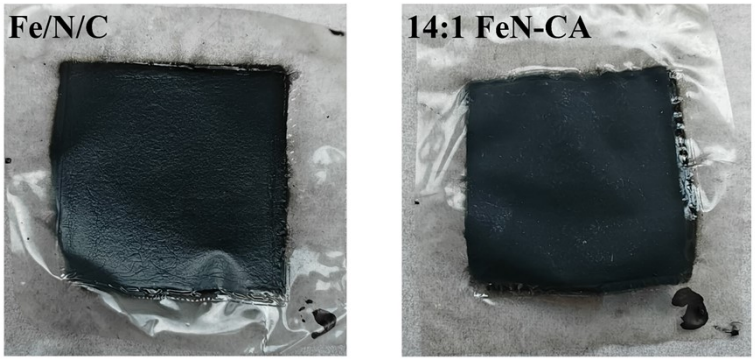

Figure S17. Image of membrane electrode after AEMFC performance test

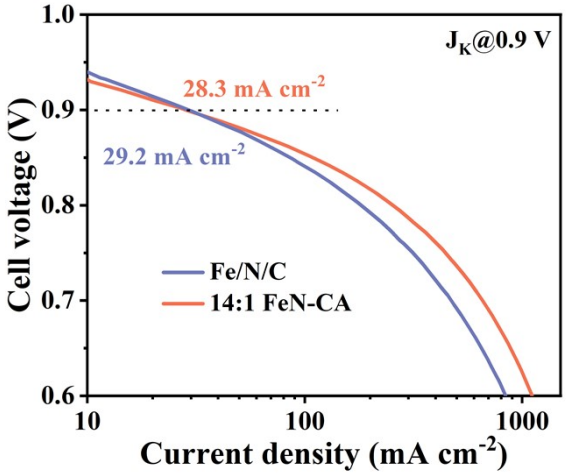

Figure S18. Comparison of JK at 0.9 V for AEMFC with both cathode and anode at 100% RH and 2.5 bar.

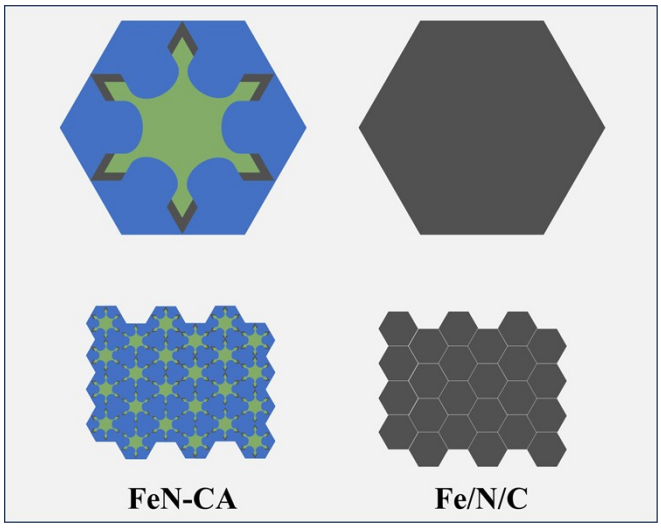

Figure S19. Finite element model (Black represents the walls and the remaining colors represent the channels).

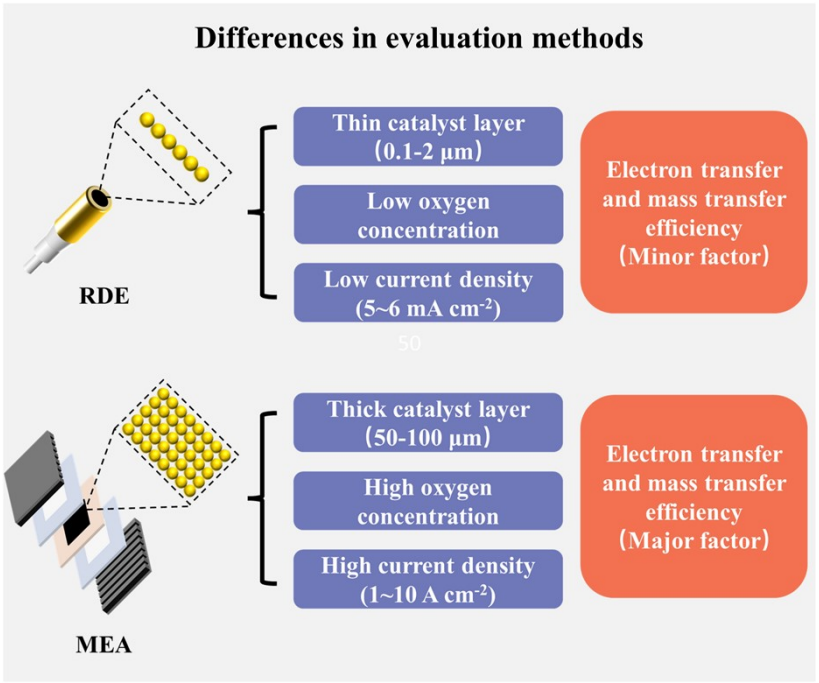

Figure S20. Differences between RDE and MEA evaluation methods.

Table S1. Elemental content from EDS mapping.

Element	C	N	O	Fe
Mass%	93.46	0.56	5.55	0.44

Table S2. Pyridinic N, Fe-N_x, pyrrolic N, graphitic N, and oxidized N contents were determined by XPS.

Sample	**Pyridinic N**	**Fe-N_x**	**Pyrrolic N**	**Graphitic N**	**N-oxide**
Fe/N/C	25.96%	12.98%	35.09%	14.74%	11.23%
14:1 FeN-CA	22.37%	14.14%	32.89%	21.38%	9.21%

Table S3. Specific surface area and pore volume of Fe/N/C catalyst and 14:1 FeN-CA catalyst in different pore structures.

14:1 FeN-CA		Pore volume		Pore area	
		$cm^3\ g^{-1}$	percent	$m^2\ g^{-1}$	percent
Micropore	0.35~2 nm	0.24	15.58%	576.98	57.91%
Mesopore	2~10 nm	0.29	19.26%	324.39	32.56%
	10~50 nm	0.29	19.10%	58.31	5.85%
Macropore	50~196 nm	0.71	46.06%	36.69	3.68%
Fe/N/C		**Pore volume**		**Pore area**	
		$cm^3\ g^{-1}$	percent	$m^2\ g^{-1}$	percent
Micropore	0.35~2 nm	0.31	30.39%	772.44	79.38%
Mesopore	2~10 nm	0.12	12.29%	156.83	16.12%
	10~50 nm	0.12	11.49%	21.84	2.24%
Macropore	50~196nm	0.47	45.83%	21.98	2.26%

Table S4. Change in the specific surface area of 14:1 FeN-CA catalyst (compared to Fe/N/C).

	Micropore	**Micropore**	**Macropore**
Pore area (vs. Fe/N/C)	-195.46	204.03	14.71
Ratio (vs. Fe/N/C)	-25.3%	114.2%	66.9%

Table S5. Comparison of Cdl and ECSA between 14:1FeN-CA Catalyst and Fe/N/C Catalyst

Sample	C_{dl} (mF cm^{-2})	ECSA (m^2 g^{-1})
14:1 FeN-CA	42.76	267.25
Fe/N/C	36.67	229.18

Table S6. PPD information for 14:1 FeN-CA and Fe/N/C.

	J (mA cm^{-2})	**PPD (mW cm^{-2})**	**Backpressure (bar)**
Fe/N/C	1341	606	2.5
14:1 FeN-CA	1724	774	2.5

Table S7. Peak power densities of 14:1 FeN-CA and Fe/N/C catalysts at 25℃ and 80℃.

	PPD (25 ℃) **mW cm^{-2}**	**PPD (80 ℃)** **mW cm^{-2}**
Fe/N/C	231	283
14:1 FeN-CA	250	383

Table S8. Summary of electrochemical performance of the previously reported ORR catalysts.

Catalysts	$E_{1/2}$ (V)	PPD (mW $g_{catalyst}^{-1}$)	Ref.
14:1 FeN-CA (80 ℃)	0.90	776	This work
14:1 FeN-CA (25 ℃)	0.90	500	This work
Hydrophobic Fe-FNC	0.8	452	[2]
FeCo-N-C-1.25	0.922	332	[3]
Fe SAs/NC	0.93	306.1	[4]
Cu-Co/NC	0.92	295.9	[5]
FeSA-N/TC	0.8	285	[6]
3D Co/N-C	0.84	239	[7]
Fe-Phen-800	0.878	222.63	[8]
NCNTM	0.85	220	[9]
Mn-SAS/CN	0.91	220	[10]
LDH-POF	0.8	185	[11]
Fe-N-C/rGO	0.9	184.69	[12]
A-MnO_2/NSPC-2	0.87	181	[13]
Co SA/NCFs	0.85	154.5	[14]
Fe/Ni-NHCS	0.92	151.3	[15]
CoSA/NCs	0.87	127.5	[16]
FeN_4B-NiN_4B	0.9	78.97	[17]
Fe-SA@PNC	0.87	74.5	[18]
Fe_1Co_3NC-1100	0.877	74.4	[19]
CoNP@FeNC-0.05	0.85	41.76	[20]

Supplementary References

[1] Y. Liu; F. Tu; Z. Zhang; Z. Zhao; P. Guo; L. Shen; Y. Zhang; L. Zhao; G. Shao; Z. Wang, *Applied Catalysis B: Environment and Energy* **2023,** *324*, 122209.

[2] C. Xu; C. Guo; J. Liu; B. Hu; H. Chen; G. Li; X. Xu; C. Shu; H. Li; C. Chen, *Small* **2023,** *19*, 2207675.

[3] H. Liu; J. Huang; K. Feng; R. Xiong; S. Ma; R. Wang; Q. Fu; M. Rafique; Z. Liu; J. Han; D. Hua; J. Li; J. Zhong; X. Wang; Z. Zhao; T. Yao; S. Jiang; P. Xu; Z. Zhang; B. Song, *Angewandte Chemie International Edition* **2024**, e202419595.

[4] Z. Li; S. Ji; C. Xu; L. Leng; H. Liu; J. H. Horton; L. Du; J. Gao; C. He; X. Qi; Q. Xu; J. Zhu, *Advanced Materials* **2022,** *35*, 2209644.

[5] Z. Li; S. Ji; C. Wang; H. Liu; L. Leng; L. Du; J. Gao; M. Qiao; J. H. Horton; Y. Wang, *Advanced Materials* **2023,** *35*, 2300905.

[6] Y. Yu; Y. Wang; F. Yang; D. Feng; M. Yang; P.-F. Xie; Y. Zhu; M. Shao; Y. Mei; J.-C. Li, *Angewandte Chemie International Edition* **2024**, e202415691.

[7] R. Wang; H. Yang; N. Lu; S. Lei; D. Jia; Z. Wang; Z. Liu; X. Wu; H. Zheng; S. Ali; F. Ma; S. Peng, *Chemical Engineering Journal* **2022,** *433*, 134500.

[8] K. Srinivas; Z. Chen; F. Ma; A. Chen; Z. Zhang; Y. Wu; M.-q. Zhu; Y. Chen, *Applied Catalysis B: Environmental* **2023,** *335*, 122887.

[9] G. Chen; Y. Xu; L. Huang; A. I. Douka; B. Y. Xia, *Journal of Energy Chemistry* **2021,** *55*, 183-189.

[10] X. Han; T. Zhang; W. Chen; B. Dong; G. Meng; L. Zheng; C. Yang; X. Sun; Z. Zhuang; D. Wang; A. Han; J. Liu, *Advanced Energy Materials* **2020,** *11*, 2002753.

[11] C. X. Zhao; J. N. Liu; B. Q. Li; D. Ren; X. Chen; J. Yu; Q. Zhang, *Advanced Functional Materials* **2020,** *30*, 2003619.

[12] L. Li; Y.-J. Chen; H.-R. Xing; N. Li; J.-W. Xia; X.-Y. Qian; H. Xu; W.-Z. Li; F.-X. Yin; G.-Y. He; H.-Q. Chen, *Nano Research* **2022,** *15*, 8056-8064.

[13] L. Huo; M. Lv; M. Li; X. Ni; J. Guan; J. Liu; S. Mei; Y. Yang; M. Zhu; Q. Feng; P. Geng; J. Hou; N. Huang; W. Liu; X. Y. Kong; Y. Zheng; L. Ye, *Advanced Materials* **2024,** *36*, 2312868.

[14] Y. Han; H. Duan; C. Zhou; H. Meng; Q. Jiang; B. Wang; W. Yan; R. Zhang, *Nano Letters* **2022,** *22*, 2497-2505.

[15] C. Zhang; X. Wang; Z. Ma; H. Yao; H. Liu; C. Li; J. Zhou; R. Xu; X. Zheng; H. Wang; Q. Li; M. Gu; H. Jiang; M. Huang, *Science Bulletin* **2023,** *68*, 2042-2053.

[16] P. Li; H. Wang; X. Tan; W. Hu; M. Huang; J. Shi; J. Chen; S. Liu; Z. Shi; Z. Li, *Applied Catalysis B: Environmental* **2022,** *316*, 121674.

[17] Z. Wang; R. Xu; Q. Ye; X. Jin; Z. Lu; Z. Yang; Y. Wang; T. Yan; Y. Liu; Z. Pan; S. J. Hwang; H. J. Fan, *Advanced Functional Materials* **2024,** *34*, 2315376.

[18] M. Shen; J. Qi; K. Gao; C. Duan; J. Liu; Q. Liu; H. Yang; Y. Ni, *Chemical Engineering Journal* **2023,** *464*, 142719.

[19] Y. He; X. Yang; Y. Li; L. Liu; S. Guo; C. Shu; F. Liu; Y. Liu; Q. Tan; G. Wu, *ACS Catalysis* **2022,** *12*, 1216-1227.

[20] Y. Xue; Y. Guo; Q. Zhang; Z. Xie; J. Wei; Z. Zhou, *Nano-Micro Letters* **2022,** *14*, 162 (2022).